SANDIA REPORT

SAND2005-6084
Unlimited Release
Printed October 2005

Measurements of Thermal Accomodation Coefficients

Daniel J. Rader, Wayne M. Trott, John R. Torczynski, Jaime N. Castañeda, and T.W. Grasser

Prepared by
Sandia National Laboratories
Albuquerque, New Mexico 87185 and Livermore, California 94550

Sandia is a multiprogram laboratory operated by Sandia Corporation,
a Lockheed Martin Company, for the United States Department of Energy's
National Nuclear Security Administration under Contract DE-AC04-94AL85000.

Issued by Sandia National Laboratories, operated for the United States Department of Energy by Sandia Corporation.

Available to DOE and DOE contractors from
U.S. Department of Energy
Office of Scientific and Technical Information
P.O. Box 62
Oak Ridge, TN 37831

Telephone: (865)576-8401
Facsimile: (865)576-5728
E-Mail: reports@adonis.osti.gov
Online ordering: http://www.osti.gov/bridge

Available to the public from
U.S. Department of Commerce
National Technical Information Service
5285 Port Royal Rd
Springfield, VA 22161

Telephone: (800)553-6847
Facsimile: (703)605-6900
E-Mail: orders@ntis.fedworld.gov
Online order: http://www.ntis.gov/help/ordermethods.asp?loc=7-4-0#online

SAND2005-6084
Unlimited Release
Printed October 2005

Measurements of Thermal Accommodation Coefficients

Daniel J. Rader, Wayne M. Trott, John R. Torczynski,
Jaime N. Castañeda, and Thomas W. Grasser
Engineering Sciences Center
Sandia National Laboratories
P. O. Box 5800
Albuquerque, New Mexico 87185-0834

Abstract

A previously-developed experimental facility has been used to determine gas-surface thermal accommodation coefficients from the pressure dependence of the heat flux between parallel plates of similar material but different surface finish. Heat flux between the plates is inferred from measurements of temperature drop between the plate surface and an adjacent temperature-controlled water bath. Thermal accommodation measurements were determined from the pressure dependence of the heat flux for a fixed plate separation. Measurements of argon and nitrogen in contact with standard machined (lathed) or polished 304 stainless steel plates are indistinguishable within experimental uncertainty. Thus, the accommodation coefficient of 304 stainless steel with nitrogen and argon is estimated to be 0.80 ± 0.02 and 0.87 ± 0.02, respectively, independent of the surface roughness within the range likely to be encountered in engineering practice. Measurements of the accommodation of helium showed a slight variation with 304 stainless steel surface roughness: 0.36 ± 0.02 for a standard machine finish and 0.40 ± 0.02 for a polished finish. Planned tests with carbon-nanotube-coated plates will be performed when 304 stainless-steel blanks have been successfully coated.

Acknowledgments

This report includes work performed under LDRD 05-1287, “Thermal Accommodation of Carbon Nanotube Coatings,” which was funded by the Laboratory Directed Research and Development (LDRD) program at Sandia National Laboratories. The efforts of Prof. Larry Overzet at the University of Texas at Dallas in developing a method to provide carbon nanotube coatings on our test plates is gratefully acknowledged.

Table of Contents

List of Figures

List of Tables

Nomenclature

Roman Variables

$\bar{c}$	mean molecular speed of a Maxwellian distribution, $\sqrt{8k_BT/\pi m}$ [m/s]
E_{in}	incident energy flux [W/m^2]
E_{re}	reflected energy flux [W/m^2]
E_w	wall-equilibrium reflected energy flux [W/m^2]
K	thermal conductivity [W/(m·K)]
k_B	Boltzmann constant [1.380658×10^{-23} J/K]
L	gap between plates [m]
m	molecular mass [kg]
P	pressure [Pa]
q	heat flux magnitude [W/m^2]
T	temperature [K]
T_c	temperature of cold wall at $x = 0$ [K]
T_h	temperature of hot wall at $x = L$ [K]
T_w	wall temperature [K]
z	Cartesian coordinate [m]

Greek Variables

α	thermal accommodation coefficient [1]
ζ	number of internal degrees of freedom [1]
λ	gas mean free path, $(2\mu)/(\rho\bar{c})$ [m]
μ	absolute viscosity [Pa·s]
ρ	mass density [kg/m^3]

Subscripts

C	continuum
FM	free molecular
wall	quantity at a solid wall boundary
c	boundary or wall at $z = 0$
h	boundary or wall at $z = L$

Acronyms

EUVL	Extreme Ultraviolet Lithography
FS	Full Scale
MEMS	Micro Electro Mechanical Systems
UTD	University of Texas at Dallas

1. Introduction

1.1. Overview

Heat transfer to surfaces immersed in noncontinuum (transitional or rarefied) gas flow continues to be an active area of research. Gases exhibit noncontinuum effects when the characteristic length scale of the system becomes comparable to the gas mean free path. Thus, these effects become important when either the system length scale becomes small (*e.g.*, Micro Electro Mechanical Systems) or when the gas pressure becomes low (*e.g.*, semiconductor manufacturing or spacecraft aerodynamics). *A priori* prediction of noncontinuum, gas-phase heat flux requires a detailed description of the gas-surface interaction. Unfortunately, and despite considerable effort over the past century, reliable gas-surface interaction mechanisms are still lacking. This gap in understanding becomes increasingly serious as modelers are asked to perform ever more sophisticated engineering analyses of systems exhibiting marked noncontinuum behavior. It is well recognized that the remedy to this dilemma lies in the development of a reliable, experimentally-validated database of gas-surface interaction models. Ideally, this database would span the wide range of gas-surface combinations that are of interest in modern engineering applications.

A previous LDRD-funded study (Rader *et al.*, 2004) took a major step toward meeting this need by developing an experimental chamber and diagnostics that can provide measurements of gas-surface thermal accommodation coefficients. The present report documents work performed under a follow-on LDRD that investigates the role of surface roughness on the thermal accommodation coefficient. The goal of this work was to measure the thermal accommodation coefficients of three very distinct surfaces: 1) mirror-polished 304 stainless steel (a *smooth* surface), 2) standard machined (by lathe) 304 stainless steel (a *moderately rough* surface), and 3) 304 stainless steel coated with a carbon nanotube forest (a *fully rough* surface). The long-term hope is to identify strategies for reliably designing surfaces that provide a specified level of thermal accommodation.

A review of gas-surface interaction theory and the details of the experimental apparatus and procedure used here are described in detail in a previous report (Rader *et al.*, 2004). Brief summaries of the salient features of this previous work are repeated here for the convenience of the reader. This chapter continues with an introduction to the problem of gas-surface interactions. Chapter 2 provides a condensed review of the underlying theory. Chapter 3 provides a short summary of the capabilities of the experimental apparatus and the test surfaces used in this work. Chapter 4 presents the most recent experimental results. Chapter 5 summarizes the work and discusses the plans for completing this study.

1.2. Motivation

The need to predict heat transfer to a surface immersed in a noncontinuum gas is common to a variety of applications of interest at Sandia National Laboratories. Gases exhibit noncontinuum effects when the characteristic length scale of the system becomes comparable to the gas mean

free path, λ, defined as the average distance traveled by a molecule between collisions. As the definition of mean free path is somewhat arbitrary, a number of definitions persist in the literature; the definition of mean free path given by Springer (1971) is used here:

$$\lambda = \frac{2\mu}{\rho \bar{c}}, \tag{1}$$

where μ and ρ are the gas viscosity and mass density, $\bar{c} = (8k_B T/\pi m)^{1/2}$ is the mean molecular speed, k_B is the Boltzmann constant, T is the local gas temperature, and m is the gas molecular mass. Noncontinuum effects become important either when system length scales become microscopically small or when gas pressures become low. The rise of noncontinuum behavior with decreasing pressure results from the inverse dependence of the mean free path on gas density, as given in Equation (1).

Applications with microscopic length scales are becoming increasingly common since the advent of Micro Electro Mechanical Systems (MEMS), which are currently manufactured with micron-scale geometric features. Microsystems are usually operated in air at ambient pressure and temperatures, for which the mean free path is ~0.065 μm (Karniadakis and Beskok, 2002). Since the mean free path is not negligibly small compared to the geometric length scales, the conduction of heat across small gas channels exhibits noncontinuum features. Thus, engineering design tools intended for thermal management analyses in microsystems must include noncontinuum capabilities. These design tools will require specific gas-surface interaction models for the materials and finishes encountered in microsystems. Device designers would benefit from the ability to select surfaces that could provide a desired level of thermal performance; *e.g.*, surfaces that are nearly insulating (low accommodation) or highly conductive (high accommodation).

Noncontinuum gas-flow effects are also encountered when the system pressure becomes small. This approach to the noncontinuum limit arises from the fact that the mean free path is inversely proportional to the gas density; thus, at sufficiently low pressures the mean free path becomes comparable even to macroscopic length scales. One long-established field of research, rarefied gas dynamics, pertains to the study of noncontinuum flow around high-speed spacecraft in the upper atmosphere. Rarefied gas flow is also observed in low-speed, low-pressure systems, such as semiconductor and MEMS manufacturing. All of these applications are of particular interest to Sandia. One of the key challenges facing the development of Extreme UltraViolet Lithography (EUVL) was the protection of the lithographic mask from particle deposition. One proposed solution was the use of thermophoretic protection, in which the mask is kept slightly warmer than a parallel plate (Klebanoff and Rader, 2000; Rader *et al.*, 2002). The flow of heat from the warmer mask to the cooler plate forces particles to move away from the mask, thereby providing protection from particle contamination. A key challenge in this design is to maximize the heat flow through the gas resulting from a given temperature difference between the mask and plate. For EUVL mask protection purposes, highly accommodating surfaces are desired.

The above applications motivated the search for a highly-accommodating surface. One possibility for achieving high accommodation is to manufacture a surface with a high degree of microscopic roughness and/or porosity. This report documents the preliminary results of an investigation of this concept.

1.3. Gas-Surface Accommodation Coefficient

Momentum and heat transfer to surfaces immersed in noncontinuum gas flows continues to be the subject of many studies since Maxwell's pioneering work over 100 years ago (Maxwell, 1890). To predict momentum and heat fluxes, it is essential to know the net balance of energy and momentum carried by molecules impinging on and reflecting from a surface. Despite considerable efforts to understand this process, detailed gas-surface interaction mechanisms are still lacking (*e.g.*, Ohwada, 1996). Consequently, *a priori* prediction of rarefied flow in simple geometries continues to be an open question.

In the absence of detailed gas-surface interaction models, theoretical predictions for stress and heat transfer usually can be brought into agreement with experimental observations by using empirical parameters called accommodation coefficients. The most widely used parameter for heat transfer is the thermal accommodation coefficient, α, which is defined by

$$\alpha = \frac{E_{in} - E_{re}}{E_{in} - E_{w}} \tag{2}$$

where E_{in} is the incident energy flux, E_{re} is the reflected energy flux, and E_{w} is the energy flux that would be achieved if the reflected molecules were emitted in thermal equilibrium at the surface temperature (Schaaf and Chambre, 1958; Springer, 1971). The thermal accommodation coefficient varies between unity (complete accommodation, diffuse reflection) and zero (adiabatic, specular reflection). The simple partition of gas-surface collisions into a diffuse, fully accommodated fraction and a specular fraction is often referred to as the *Maxwell wall model*, a convention which is followed in this work. Note that Equation (2) represents an average over a finite area of surface and a very large number of gas-surface collisions. Also, no attempt is made to distinguish among the possibly different accommodations for the various molecular degrees of freedom. Thus, the net flux of translational energy is lumped together with that of rotational and vibrational energy, if present. Experimental data related to the separate contributions to the accommodation coefficient of the different energy modes are virtually nonexistent.

Previous experimental studies have measured the thermal accommodation coefficient in a variety of geometries and over a wide range of gas-surface combinations. Springer (1971) presents some typical values while an extensive review is available in Saxena and Joshi (1989). The data show that accommodation strongly depends on the composition and temperature of the gas and surface, on gas pressure, and on the state of the surface (roughness, contaminant adsorption, gas adsorption). Experimental values reported for the thermal accommodation coefficient range from 0.01 to nearly unity, depending on the gas-surface combination and the level of contaminant gas layers adsorbed on the surface. The smaller values tend to be observed for light gases striking surfaces composed of higher-atomic-weight molecules (*e.g.*, helium striking a clean tungsten surface); near unity values tend to be observed for heavy gases striking lower- or similar-molecular weight or contaminated surfaces (*e.g.*, on tungsten). Qualitative theoretical arguments predict that thermal accommodation tends to increase with increasing gas molecular weight and with roughness for a given surface. A key limitation of the existing data base, however, is the lack of accommodation data for surfaces encountered in present-day MEMS devices.

2. Theory

2.1. Overview

In this study, the gas-surface thermal accommodation coefficient is inferred from experimental measurements of the pressure dependence of gas heat flux between two parallel plates of unequal temperature. The gas-phase conduction of heat between infinite parallel plates is often referred to as the Fourier problem and has received considerable theoretical treatment in the literature because of its geometric simplicity. The following chapter reviews this theoretical literature with a particular emphasis on those results which are of use in interpreting the experimental results that will be presented later (for more details, see Rader *et al*., 2004).

2.2. Fourier Geometry

The classic Fourier geometry is defined by a quiescent gas occupying the region between two infinite, parallel plates of unequal temperature. A schematic diagram of this geometry is shown in Figure 1. The two plates are separated by a gap, L, and the coordinate system is defined such that $z = 0$ corresponds to the surface of the bottom plate. The temperature of the top plate, T_h, is assumed (without loss of generality) to be higher than that of the lower plate, T_c. In the experiments, these two temperatures do not differ by much, so the assumption $T_h - T_c \ll T_c$ is typically satisfied. Because of the imposed temperature difference, heat is conducted through the gas from the hot plate to the cold plate. The theoretical analyses assume that the gas is quiescent (no mass flow); consequently, the gas-phase heat transfer between the plates is dominated by conduction, and convection is neglected. Radiation is not treated theoretically in this chapter but is considered in the experimental analysis.

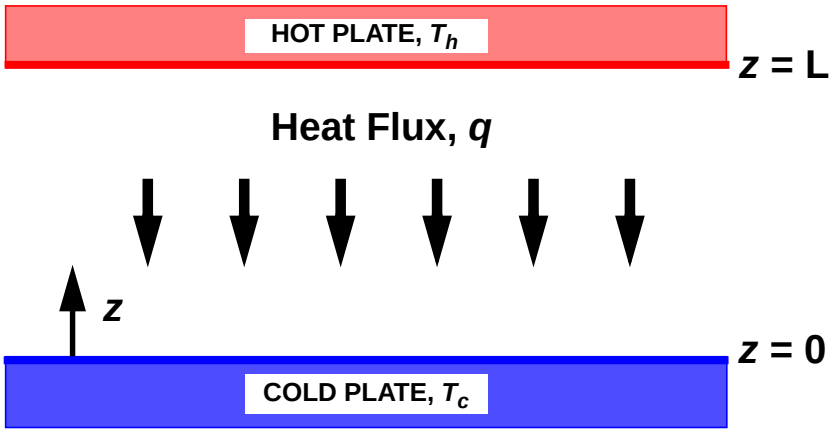

Figure 1. Schematic diagram of the Fourier heat conduction geometry.

2.3. Surface Accommodation Model

A Maxwell (1890) wall model is considered in this study. In the Maxwell model, a fraction, α, of molecules is reflected diffusely with complete thermal accommodation, while the remaining fraction of molecules, $1-\alpha$, is assumed to be reflected specularly. Molecules undergoing a diffuse reflection possess a half-range Maxwellian molecular velocity distribution in equilibrium with the wall temperature. For a specular reflection, the tangential velocity of a molecule is left unchanged while the normal velocity changes sign but not magnitude. A purely diffuse surface would be characterized by $\alpha = 1$, a purely specular surface would have $\alpha = 0$, while in the general case the surface accommodation coefficient would lie somewhere in between, $0 \le \alpha \le 1$.

As discussed in Chapter 1, the Maxwell wall model is undoubtedly overly simplistic, but it is in fact this simplicity that has made this model so popular for correlating experimental observations. In general, each wall would be expected to be characterized by a separate accommodation coefficient. Thus, α_h would be associated with the hot wall, and α_c with the cold wall. In practice, however, the experiments presented below are performed with the careful intent to maintain the materials and surface finishes of the two plates as similar as possible. In this case, the assumption is made that there is only one accommodation coefficient, $\alpha = \alpha_h = \alpha_c$.

2.4. Gas-Phase Heat Conduction

In the free molecular limit ($\lambda >> L$) molecules travel back and forth between the plates without colliding with each other; in this case the heat transfer between the plates can be described from a molecular point of view. In the free molecular limit, the space between the walls is characterized by two streams of non-collisional molecules, with higher-energy molecules streaming downward from the hot plate and lower-energy molecules streaming upward from the cold plate. For a stationary gas with ζ internal degrees of freedom, Bird (1994, p. 84) has shown that the total heat flux to a surface is increased by a factor of $(1 + \zeta/4)$ compared to the translational heat flux. Thus, Bird's (1994, p. 280) monatomic-gas result for the free molecular heat flux, q_{FM}, can be extended to a polyatomic gas for the case of small temperature differences and equal wall accommodation coefficients:

$$q_{FM} = -\frac{1}{2}\left(\frac{P\bar{c}}{T}\right)\left(\frac{\alpha}{2-\alpha}\right)\left(1+\frac{\zeta}{4}\right)(T_h - T_c), \qquad \begin{matrix}\alpha_h = \alpha_c = \alpha \\ T_h - T_c \ll T_c\end{matrix}, \tag{3}$$

where $T = T_h^{1/2} T_c^{1/2}$ and the approximation $T_h^{1/2} + T_c^{1/2} \approx 2T^{1/2}$ has been used. The free molecular heat flux is directly proportional to the gas pressure, P; in the limit of vanishing pressure, the heat flux approaches zero, as it must in a vacuum. No gradients in macroscopic gas properties are observed in the free molecular limit: the temperature is constant across the domain with a value equal to the geometric mean of the two wall temperatures, $T = T_h^{1/2} T_c^{1/2}$.

In the continuum limit ($\lambda << L$), the energy equation is satisfied using the well-known Fourier heat conduction law. In this case, the continuum heat flux, q_C, is given by

$$q_C = -K(T)\frac{dT}{dz}, \tag{4}$$

where K is the gas thermal conductivity which depends on temperature. Equation (4) applies equally well for any gas (*i.e.*, monatomic, diatomic) if the appropriate value of K is used. The one-dimensional nature of the Fourier geometry requires that the heat flux be constant across the domain (independent of z). Note that the thermal conductivity is independent of pressure; hence, the heat flux is also independent of pressure as long as the flow lies in the continuum regime. For small temperature variations, the thermal conductivity can be assumed to be constant, and Equation (4) can be integrated to obtain:

$$q_C = -K\left(\frac{T_h - T_c}{L}\right), \qquad T_h - T_c \ll T_c \quad . \tag{5}$$

The prediction of the heat flux in the transition regime that lies between the free molecular and continuum limits is challenging, ultimately requiring a complete solution of the Boltzmann equation. Although many theoretical analyses are available in the literature (for a review, see Springer, 1971), few result in closed-form expressions for the heat flux. One exception is the analysis of Liu and Lees (1961), who used a four-moment solution of the linearized Boltzmann equation for a monatomic gas to derive an approximate, closed-form expression for the heat flux. Springer (1971) extended Liu and Lees' analysis to polyatomic gases and presented the following expression for the heat flux, q, which is intended to apply over the entire pressure range:

$$\frac{q}{q_C} = \frac{1}{1 + \dfrac{q_C}{q_{FM}}} = \frac{1}{1 + \dfrac{2KT}{L\left(\dfrac{\alpha}{2-\alpha}\right)\left(1 + \dfrac{\zeta}{4}\right)\bar{c}P}}, \qquad \begin{matrix} \alpha_h = \alpha_c = \alpha \\ T_h - T_c \ll T_c \end{matrix} \quad , \tag{6}$$

where $\bar{c} = (8k_BT/\pi m)^{1/2}$. Springer (1971) has shown that Equation (6) agrees reasonably well with the limited available experimental data for monatomic and diatomic gases over a wide range of conditions. Independently, Sherman (1963) suggested a simple interpolation formula for heat flux that has the same form as Equation (6), except that he allowed the continuum and free molecular heat fluxes to be calculated from their complete (not linearized) expressions. For convenience, Equation (6) is referred to as the "Sherman-Lees" interpolation formula for heat flux.

For analysis of the experimental data to be presented later, it is convenient to rewrite Equation (6) in the following form:

$$\frac{1}{q} = \frac{1}{q_C} + \frac{1}{q_C} \cdot \frac{2KT}{L\left(\dfrac{\alpha}{2-\alpha}\right)\left(1 + \dfrac{\zeta}{4}\right)\bar{c}} \cdot \frac{1}{P}. \tag{7}$$

3. Experimental Apparatus and Procedure

3.1. Overview

This chapter provides a brief description of the design and operation of the vacuum test chamber and diagnostics used in the present study (see Rader *et al.*, 2004). The vacuum test chamber was designed to accommodate all of the control systems and diagnostics needed to provide heat-flux measurements between two parallel, 14.25-cm-diameter plates. Heat flux between the plates is inferred from temperature-drop measurements between precision thermistors embedded near the exposed surface of each plate and those immersed in an adjacent water plenum. To provide a high degree of accuracy, state-of-the-art components were selected for controlling system pressure, flow rate, plate alignment, plate temperatures, plate positions, system pressure, and system temperature.

3.2. Vacuum Test Chamber and Environmental Control Systems

A schematic of the vacuum test chamber design is shown in cross section in Figure 2. The test chamber is a 41-cm-diameter sphere with six 33.66-cm (13.25-in) OD standard conflat flanges welded as shown. The opposing upper and lower flanges were used to mount the upper and lower plate assemblies. An observation window (optical-quality quartz) occupies the flange extending out of the plane in Figure 2. A photograph of the test chamber and associated support systems is shown in Figure 3.

Stable control and accurate measurement of gas conditions in the test chamber are essential prerequisites for making the measurements desired in this project. Pressure measurements are made using five state-of-the-art, MKS 690A high-accuracy Baratron pressure transducers (0.05% of full scale). Chamber pressure is actively controlled by comparing the Baratron-measured pressure with an operator-selected pressure set-point; an MKS 244E pressure/flow controller maintains the desired pressure by regulating the flow into the chamber through an automated MKS 245 proportioning control valve. Tests show that the flow controller provides exceptionally stable chamber pressures; for example, the system can maintain a pressure of 30.00 ± 0.01 mTorr over long periods of operation. Thus, the pressure-measurement and flow-regulation subsystems provide extremely accurate and precise control.

3.3. Plate Assemblies

Significant care was given to the design of the assemblies which hold the test plates (whose working surfaces are in contact with the gas and determine the gas/surface interface). The plate assemblies were designed to meet several aggressive requirements: 1) maintain a constant temperature across the test plate, 2) precisely position each plate surface independently, 3) maintain parallel alignment between the two plates, 4) provide thermistor access for heat-flux measurements, and 5) allow for ~1-day interchange of plates.

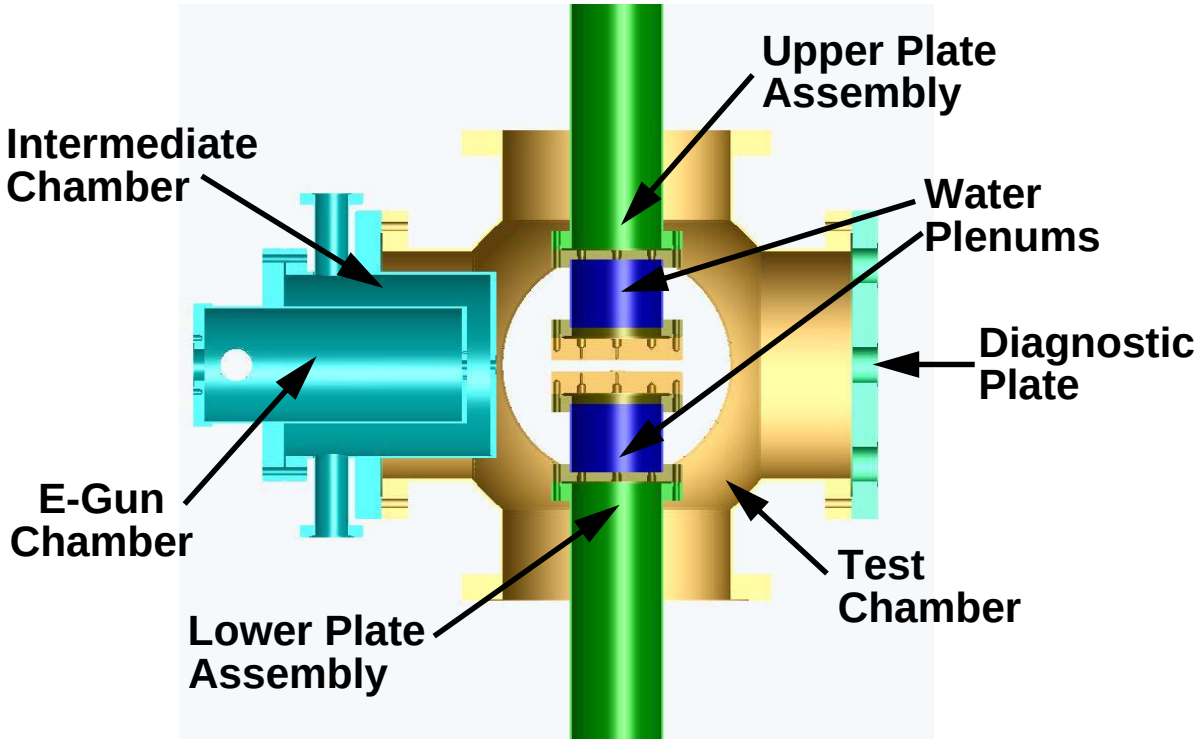

Figure 2. Schematic diagram of the test chamber.

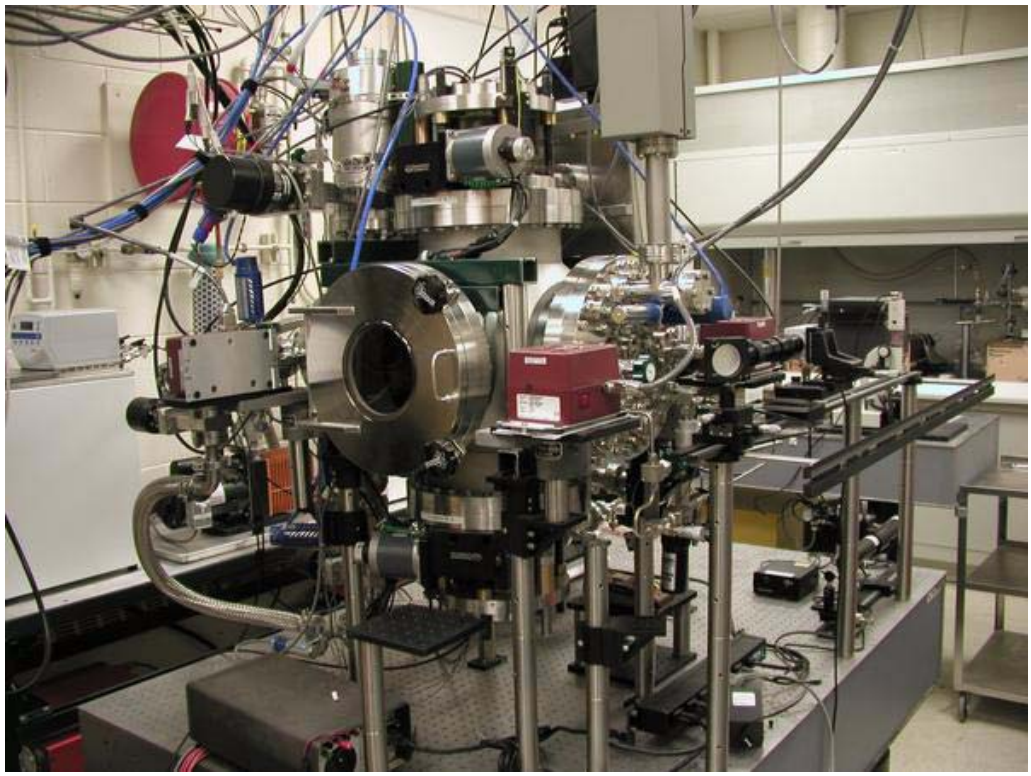

Figure 3. Front view of assembled test chamber (observation window in foreground).

To provide interchangeability, the test plates are based on a 6-inch conflat flange that was reduced to a 14.27-cm OD. The experiments reported here use 2.54-cm-thick, 304 stainless steel conflat flanges whose surfaces are treated in several ways (see below). The test plate is secured to a "spool" assembly, which provides direct contact between a 0.62-liter plenum of water and the back side of the test plate (see Figure 4). Two temperature-controlled water baths provide independent control of the temperature of the upper and lower water plenums. Three high-precision Hart Scientific thermistors (stated accuracy 0.01°C) are embedded to within ~1.6 mm of the surface of each test plate: one thermistor is centered, while the other two are positioned at a radius of 1.5 inch (3.8 cm). One thermistor is submerged within the water plenum of each spool. The embedded thermistors are used to measure plate temperature and to check for uniformity, while the difference between the centered, embedded thermistor and the submerged, bath thermistor is used to infer heat flux (see below). The thermistors are precise (repeatable) to better than 0.005°C in day-to-day operations. It is this extremely high degree of measurement precision that enables the accurate heat-flux measurements that are described below.

The spool assemblies are mounted to extension columns (see Figure 2) and extensible metal bellows that seal to the top and bottom flanges of the test chamber. The vertical position of each plate assembly is controlled by a separate precision positioner (Thermionics). These positioners can adjust the vertical position of the ~20-kg plate assemblies independently with ~10-micron accuracy. Software is used to control the position of each plate assembly independently or to operate the two positioners in a master/slave mode to maintain a fixed distance between the plates.

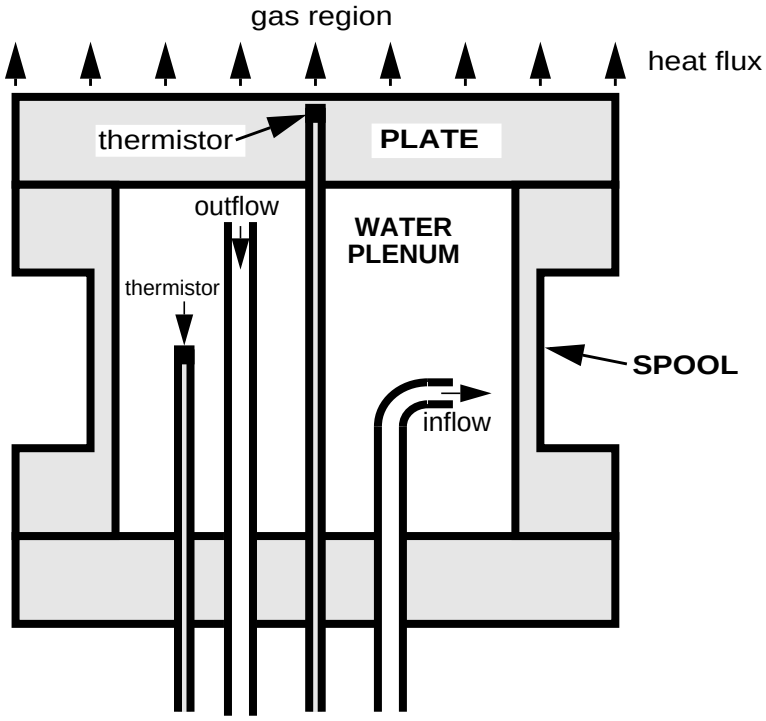

Figure 4. Elements of temperature-drop measurements in the "spool" assembly.

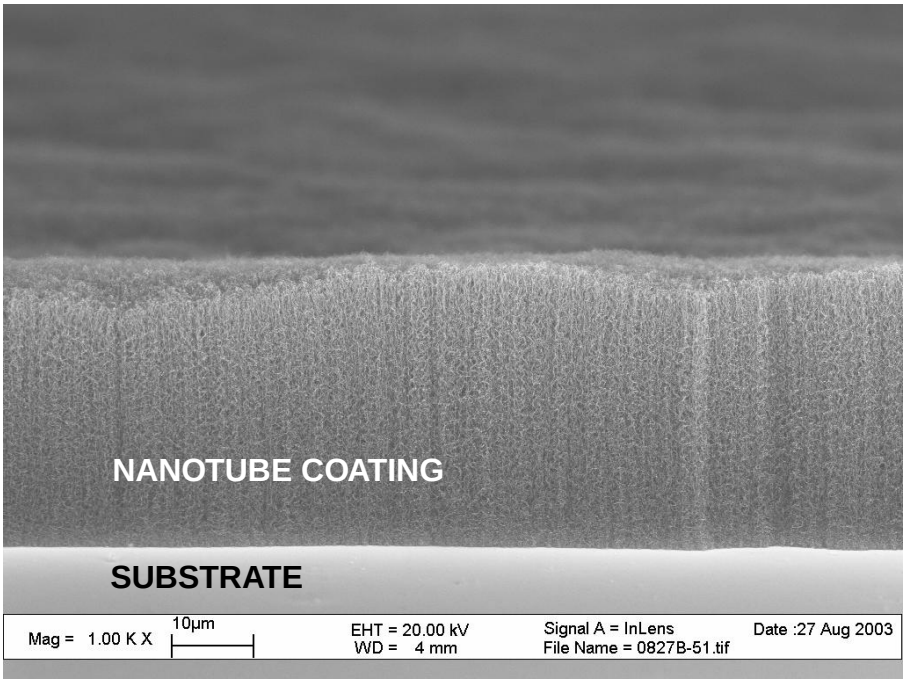

Figure 5. Carbon-nanotube coating (image courtesy of Prof. L. Overzet, UTD).

3.4. Test-Plate Surface Preparations

All of the surfaces tested to date are based on a 2.54-cm-thick, 304 stainless steel conflat flange. In previous work (Rader *et al.*, 2004), two plates were prepared with a standard machined (lathed) surface with an RMS roughness of ~2 μm. These plates were installed in the test chamber, and their thermal accommodation coefficient was inferred from heat-flux measurements as described below. For this investigation, four additional 304 stainless steel plates were prepared with the same standard machined surface. Two of these plates were subsequently polished at the Sandia shops to achieve a mirror finish characterized by an RMS roughness of ~20 nm — a hundred-fold reduction in surface roughness. Measurements of the thermal-accommodation coefficient of these two polished plates are presented below. The final two plates were shipped to the University of Texas at Dallas (UTD) to be coated with carbon nanotubes. An example of the fractal-like morphology that can be achieved with a carbon-nanotube coating is shown in Figure 5 (microphotograph courtesy of L. Overzet, UTD). These plates have not yet been coated due to the difficulty in uniformly coating such a large area. It is expected that the remaining challenges will be overcome and carbon-nanotube-coated plates returned for testing in the fall of 2005.

3.5. Heat-Flux Measurements

Temperature-difference measurements are used to infer the axial heat flux between the two test plates (Rader *et al.*, 2004). For this purpose, the temperature difference of interest is between a central thermistor embedded just beneath the test-plate working surface and another immersed in the adjacent water plenum (see Figure 4). This is a challenging measurement strategy, as the heat flux through a low-pressure gas is known to be extremely small. The measurement is further complicated by the fact that the thermal conductivities of solids and liquids are very large compared to those of gases. Consequently, the temperature differences across the water plenum and stainless steel plate are found to be extremely small but measurable given the high precision of the Hart thermistors (Rader *et al.*, 2004).

As an example, Figure 6 shows measured temperature (top) and temperature-difference (bottom) histories for nitrogen coupled with the machined 304 stainless steel plates. The test was conducted with an inter-plate gap of 5 mm and bath temperatures of 15°C and 35°C (approximately symmetric about room temperature). Thermistor readings were recorded with the chamber held near vacuum (left side of the plots) and at pressures between 1 and 6700 mTorr (series of steps moving to the right side of the plots). Histories are shown only for the hot (top) plate. Only the temperatures recorded by the center embedded and the immersed thermistors are shown in Figure 6 (top).

The accurate determination of heat flux based on temperature measurements assumes that the temperature difference between the embedded and immersed thermistors is linearly proportional to the axial heat flux. Taking advantage of symmetry, the difference between the temperatures of the central embedded thermistor, T_{center}, and the immersed thermistor, T_{im}, is considered. Temperature-difference histories for the data are presented in Figure 6 (bottom), where the magnitude of the differences is $\left|T_{\text{center}} - T_{\text{im}}\right|$. One immediate observation is that the pressure steps are now much more clearly identifiable than in Figure 6 (top). This improvement in signal is a result of the difference operation, which removes intermediate- and long-term drifts in the liquid-plenum temperature. Although these drifts are reasonably small (~0.05°C over 5 hours), they act to conceal the true trend of the temperature differences. For constant conditions (*e.g.*, fixed pressure, gap, plate temperatures), averaging the temperature difference over time (30-60 minutes) significantly improves the signal-to-noise ratio of the measurements. Using time averaging, the current apparatus can resolve temperature-difference steps as small as ~0.001°C. For example, when pressure is changed from 1 to 3 mTorr, the measured temperature difference increases by 0.009°C, about one order of magnitude larger than the minimum resolution (see Figure 6). Clearly, very small changes in heat flux can be resolved with the current system.

The next step in determining gas-phase conduction is to subtract parasitic heat losses which are always present in the system but can be observed in isolation at vacuum. In the absence of gas, any heat flux through the test plates must result from either radiation or solid conduction. For the present apparatus, it is believed that the majority of the parasitic loss results from radiation. Thus, in the following discussion, parasitic losses observed under vacuum are attributed to radiation. Radiation heat losses are clearly evident in Figure 6 for the 0 mTorr cases; for the top plate, this

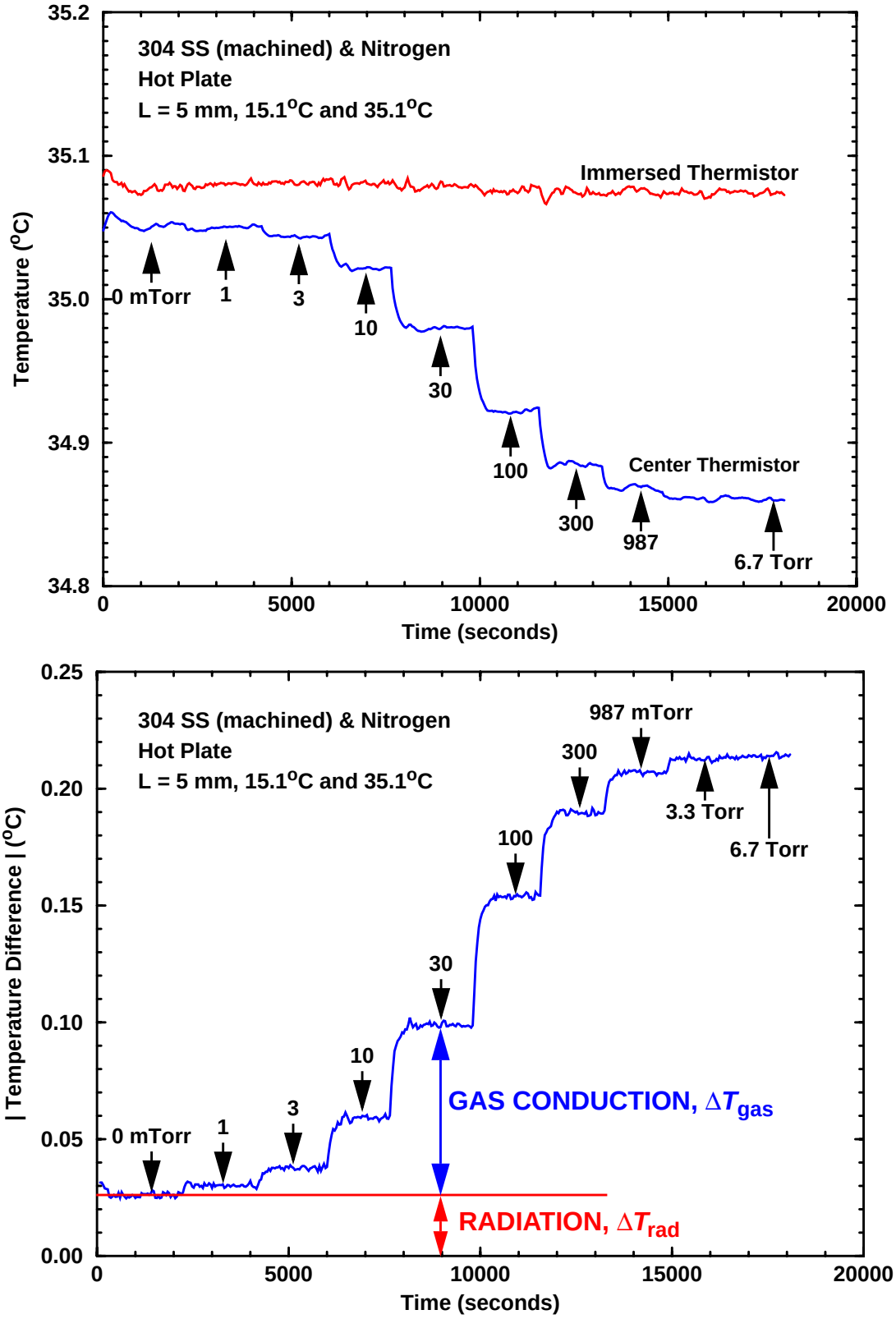

Figure 6. Temperature (top) and temperature-difference (bottom) histories for the hot plate (nitrogen, machined 304 stainless steel, 5-mm gap).

heat-loss contribution is labeled “RADIATION” in the figure and gives a temperature difference of $\Delta T_{\text{rad}} = 0.026^{\circ}\,\text{C}$. The temperature-difference contribution from gas-phase conduction, ΔT_{gas}, is determined by subtracting the temperature difference observed under vacuum, ΔT_{rad}, from the total temperature difference:

$$\Delta T_{\text{gas}} = \Delta T - \Delta T_{\text{rad}}. \tag{8}$$

Although the radiation contribution is much smaller than gas-phase conduction at higher pressures, at pressures below a few mTorr radiation dominates.

The final step in determining heat flux from temperature-difference measurements is to establish a calibration point. One possibility is suggested by the high-pressure data of Figure 6, which clearly show that the measured temperature difference plateaus for pressures above ~5 Torr. The explanation for this behavior is that the continuum limit has been achieved, for which gas-phase heat conduction becomes independent of pressure. The continuum heat flux, q_C, can be accurately calculated using Equation (4), the plate separation, and gas properties (see Chapter 2). Heat flux at arbitrary pressures can be determined by a simple scaling:

$$\frac{q}{q_C} = \frac{\Delta T_{\text{gas}}}{\Delta T_C}, \tag{9}$$

where

$$\Delta T_C = \lim_{P \to \infty} (\Delta T_{\text{gas}}) = \lim_{P \to \infty} (\Delta T - \Delta T_{\text{rad}}). \tag{10}$$

Given that ΔT_{gas} is proportional to heat flux, q, it is possible to rewrite Equation (7) in a form that is convenient for data analysis:

$$\frac{1}{\Delta T_{\text{gas}}} = \frac{1}{\Delta T_C} + \frac{1}{\Delta T_C} \cdot \frac{2KT}{L\left(\frac{\alpha}{2-\alpha}\right)\left(1+\frac{\zeta}{4}\right)\bar{c}} \cdot \frac{1}{P}. \tag{11}$$

Equation (11) is not rigorous, being based on two assumptions: 1) that the Sherman-Lees interpolation formula correctly describes the pressure-dependence of gas heat flux, and 2) that the measured temperature differences are linearly related to the axial heat flux. Nevertheless, Equation (11) is proposed as a means of correlating the experimental measurements of ΔT_{gas} as a function of pressure. The form of Equation (11) suggests that a plot of $1/\Delta T_{\text{gas}}$ against inverse pressure, $1/P$, should be linear. A graphical interpretation of such a plot is that the *y*-axis intercept equals the reciprocal of the continuum-limit temperature difference, ΔT_C, and the slope is a function of known quantities and the accommodation coefficient. Thus, regression of data such as are shown in Figure 6 can be used to determine a best-fit value for the slope from which the accommodation coefficient is extracted. For more details, see Rader *et al.* (2004).

4. Experimental Results

4.1. Overview

This chapter presents data from tests of *machined* and *highly-polished* 304 stainless steel in contact with helium, argon, and nitrogen. Thermal accommodation coefficients are determined from the pressure dependence of the heat flux (inferred from the temperature drop between the bath-immersed and plate-embedded thermistors) as described in the previous chapter.

4.2. Accommodation of Gases with Machined 304 Stainless Steel

Measurements of ΔT_{gas} as a function of pressure are made for machined 304 stainless steel plates in contact with helium, argon, and nitrogen (see also Rader *et al.*, 2004). Two plates were prepared with a standard machined (lathed) surface, and both had a measured RMS roughness of ~2 μm. For each gas-plate combination, several tests are performed using different combinations of plate separation and hot and cold plate temperatures. The data have been analyzed in the manner described in Chapter 3 and plotted in the form suggested by Equation (11). For example, the raw data for nitrogen shown in Figure 6 (5-mm gap, $T_c = 15.1°\text{C}$ and $T_h = 35.1°\text{C}$) are replotted in Figure 7 for the pressure range $30 < P < 6700$ mTorr ($4.0 < P < 893.3$ Pa). Data for both the cold (bottom) and hot (top) plates are shown. The linear nature of the data when plotted in this fashion is clearly evident. Linear regressions to the data from each plate give correlation coefficients near unity, $r^2 = 0.99999$: the reciprocal of the intercept and the slope are given in Table 1. The reciprocal of the regression intercepts give continuum-limit temperature differences of $\Delta T_C = 0.2152$ and 0.1895 °C for the cold and hot plates, respectively. Inspection of the top-plate temperature histories plotted in Figure 6 reveals that the 6.7-Torr measurement has reached 99% of the continuum limit.

The regression slopes can be used to determine the thermal accommodation coefficient according to Equation (11). The resulting values for the cold and hot plate, $\alpha = 0.808$ and 0.795, respectively, are in excellent agreement. This is a satisfying result, as the heat flux between the two plates should be exactly equal in the ideal one-dimensional situation where parasitic heat losses and nonlinearities can be neglected. The determination of thermal accommodation for gas/surface interactions is the goal of this experiment. The results reported here are consistent with a Maxwell wall model in which 80% of nitrogen molecules undergo a diffuse, thermally-accommodated reflection, while the remainder undergo a specular reflection. Moreover, the good agreement between data and regression in Figure 7 suggest that the Sherman-Lees interpolation function works exceptionally well in the near-continuum regime.

Similar tests are repeated with the machined 304 stainless steel plates with argon and helium. The conditions used for the argon tests are: 10-mm gap, $T_c = 5.2°\text{C}$ and $T_h = 45.0°\text{C}$. The conditions used for the helium tests are: 10-mm gap, $T_c = 20.2°\text{C}$ and $T_h = 30.1°\text{C}$. The data from these two tests are analyzed in the manner described above and plotted in the pressure ranges

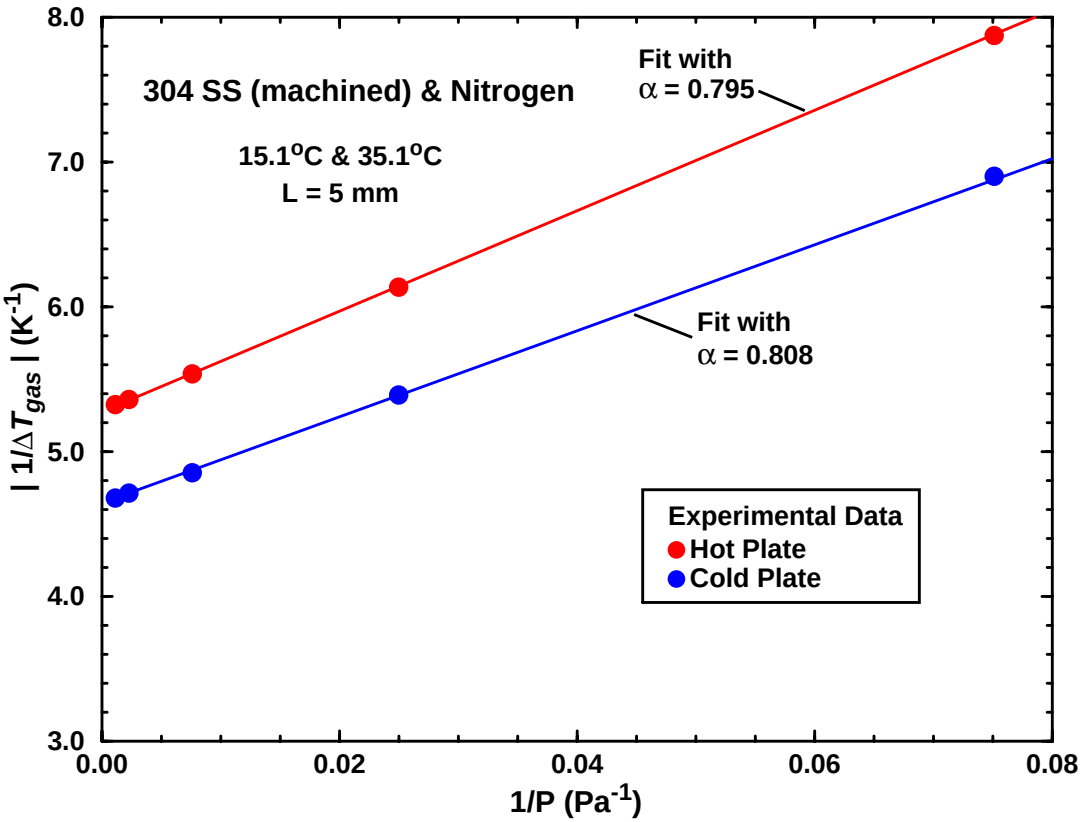

Figure 7. Plot of inverse ΔT_{gas} vs. inverse pressure in the temperature-jump regime (nitrogen, T_c = 15.1°C, T_h = 35.1°C, machined 304 stainless steel, 5-mm gap).

$50 < P < 10000$ mTorr ($6.7 < P < 1333.2$ Pa) for argon and $200 < P < 10000$ mTorr ($26.7 < P < 1333.2$ Pa) for helium. The results are plotted in Figure 8 for the both the cold and hot plates. As before, the linear nature of the data when plotted in this fashion is clearly evident, with correlation coefficients near unity. The reciprocals of the intercepts and the slopes are given in Table 1. The accommodation coefficients calculated for argon for the cold and hot plates, $\alpha = 0.875$ and 0.866, respectively, are in good agreement. The accommodation coefficients calculated for helium for the cold and hot plates, $\alpha = 0.363$ and 0.360, respectively, are also in good agreement.

Based on these and additional tests, the best accommodation coefficients for helium, nitrogen, and argon in contact with machined 304 stainless steel is determined to be $\alpha = 0.36$, 0.80, and 0.87, respectively, with an estimated uncertainty of ± 0.02 for each value. As suggested by qualitative physical arguments, the accommodation coefficient increases with increasing gas molecular weight. For helium, only about one third of the wall collisions transfer heat, while for the heavier gases the fraction is closer to unity.

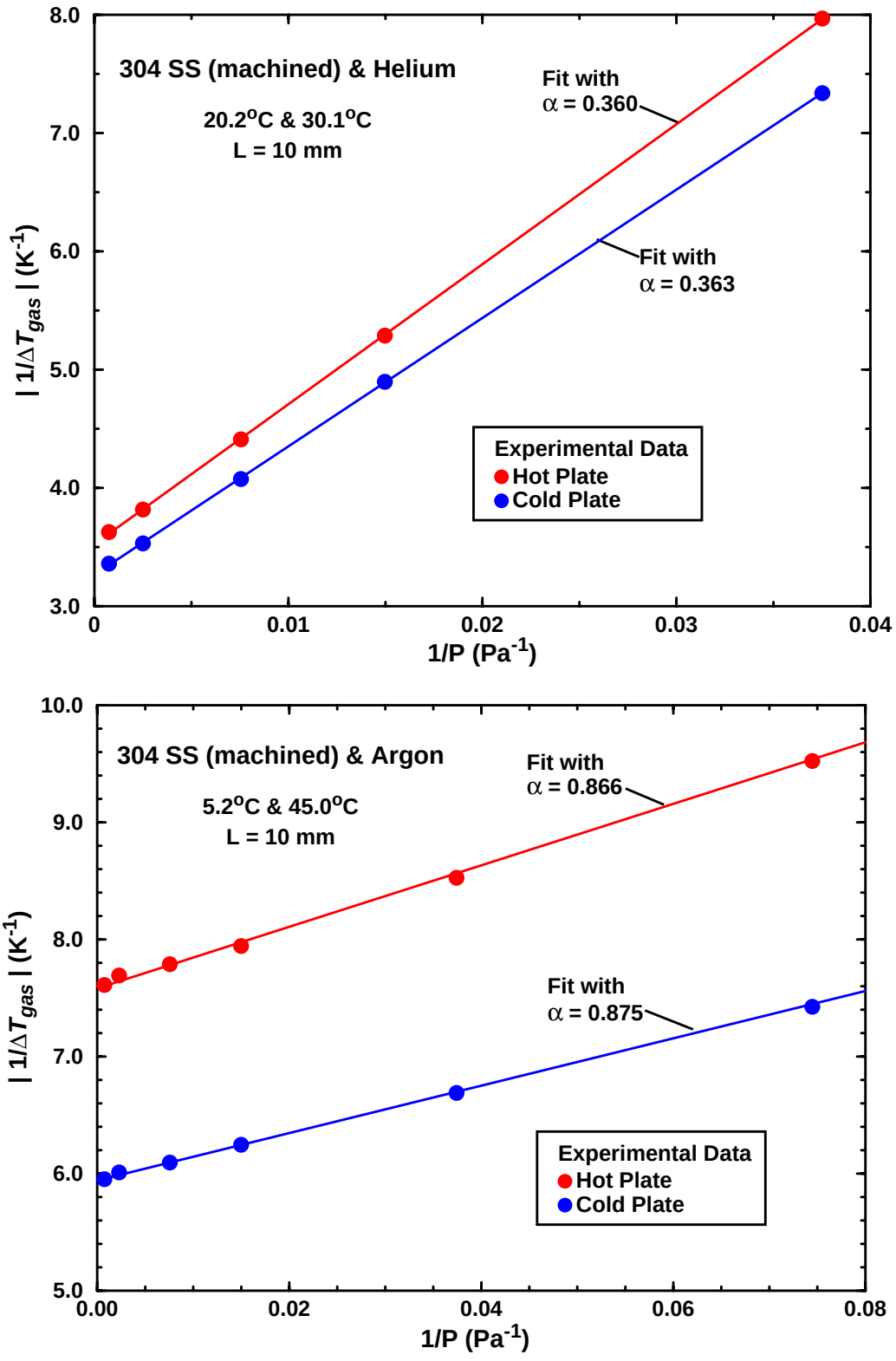

Figure 8. Plot of inverse ΔT_{gas} vs. inverse pressure in the temperature-jump regime for helium (top) and argon (bottom).

4.3. Accommodation of Gases with Polished 304 Stainless Steel

Measurements of ΔT_{gas} as a function of pressure are presented for *polished* 304 stainless steel plates in contact with helium, argon, and nitrogen. The plates were essentially identical to the plates described in the previous section but are hand polished to obtain a mirror finish (measured surface roughness, ~20 nm). Polished plates tests are performed under the same conditions (plate temperatures and separation) as in the previous section with the same three gases: helium, argon, and nitrogen. As before, inverse temperature difference is plotted against inverse pressure, and the thermal accommodation coefficient is determined from the slope of the line. For comparison, the cold-plate results from both the machined- and polished-plate tests are shown below (hot-plate results are comparable). The best-fit slopes and intercepts are given in Table 1.

The results for argon and nitrogen are shown Figure 9. For both gases, the machined and polished curves are substantially parallel, which implies that the accommodation coefficients are similar. The accommodation coefficients for argon in contact with the machined and polished plates are found to be $\alpha = 0.865$ and 0.875, respectively. The accommodation coefficients for nitrogen in contact with the machined and polished plates are found to be $\alpha = 0.808$ and 0.800, respectively. For each gas, the machined- and polished-plate accommodation coefficients agree within experimental uncertainty, ± 0.02. Thus, for argon and nitrogen, the effect of surface roughness on accommodation is smaller than can be detected in this experiment. This result is surprising considering the factor of 100 difference in surface roughness between the two surfaces. Given that these two surfaces generally span the range of surfaces roughness that can be obtained using conventional machining processes with 304 stainless steel, the preliminary conclusion drawn here is that thermal accommodation coefficient for argon and nitrogen combined with 304 stainless steel are 0.87 and 0.80, respectively, independent of surface roughness. Clearly, additional tests are warranted to test this hypothesis. One interesting point to note is that both polished-plate tests exhibit a different *x*-axis-intercept than the machined-plate tests. Since the *x*-intercept is related to the reciprocal of the continuum heat flux, which is independent of accommodation, this result is unexpected. Although the shift is small, ~6%, it suggests a systematic error in the measurements. Candidates include side-wall parasitic heat losses and uncertainties in the inter-plate separation arising from chamber flexure under vacuum; both of these issues are being addressed in planned upgrades to the experimental chamber.

The results for helium in contact with the machined and polished plates are shown separately in Figure 10. These results are qualitatively distinct from the argon and nitrogen data in two regards. First, the *x*-intercept of the two curves are found to be in very good agreement, suggesting that the heat fluxes in these two tests approach the same continuum limit. Unlike the nitrogen and argon results, however, the slopes for the two helium experiments are clearly distinguishable, implying distinct accommodation coefficients for the two different surfaces. Calculation of accommodation coefficients from the slopes gives values for the machined and polished plates of $\alpha = 0.363$ and 0.409, respectively. Thus, although the observed difference is only slightly larger than experimental uncertainties, it appears that there is a small effect of surface roughness on the thermal accommodation of helium with 304 stainless steel. A good estimate for helium would be $\alpha = 0.36$ with rough 304 stainless steel, and $\alpha = 0.40$ with polished 304 stainless steel.

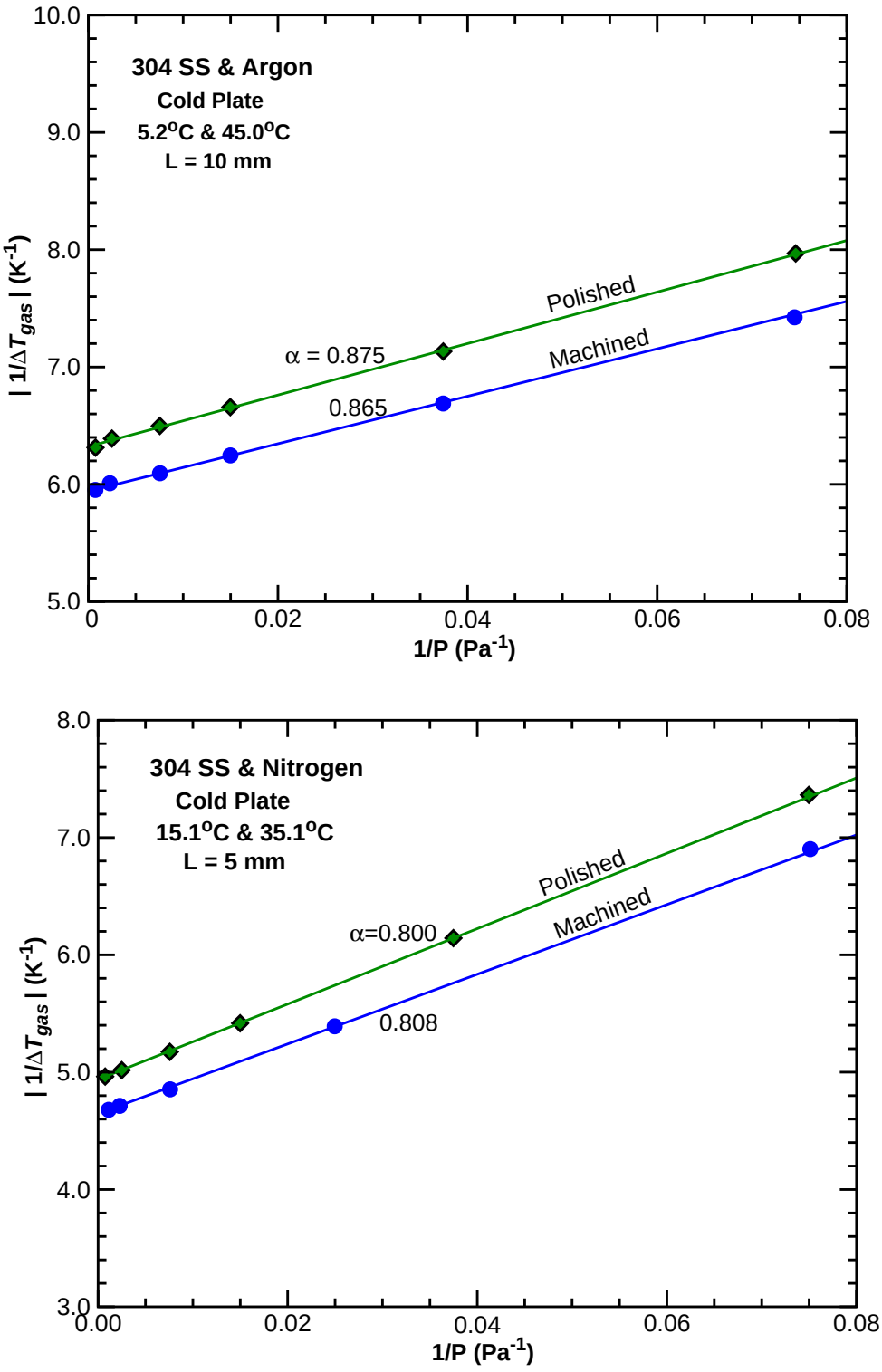

Figure 9. Plot of inverse ΔT_{gas} vs. inverse pressure for machined and polished 304 stainless steel. *Top:* argon, T_c = 5.2°C, T_h = 45.0°C, 10-mm gap. *Bottom:* nitrogen, T_c = 15.1°C, T_h = 35.1°C, 5-mm gap.

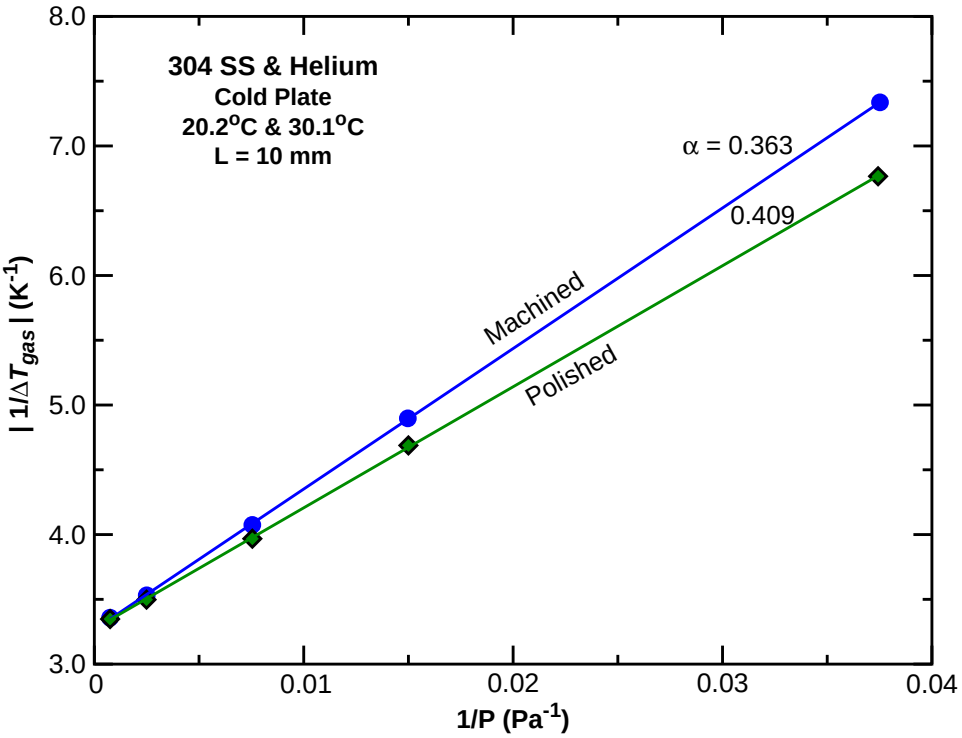

Figure 10. Plot of inverse ΔT_{gas} vs. inverse pressure for machined and polished 304 stainless steel: helium, T_c = 20.2°C, T_h = 30.1°C, 10-mm gap.

4.4. Summary of Heat-Flux and Accommodation Measurements

Table 1. Summary of heat-flux and accommodation measurements

Gas, L, T_c/T_h	Cold (bottom) Plate			Hot (top) Plate		
	ΔT_C (K)	slope (Pa/K)	α	ΔT_C (K)	slope (Pa/K)	α
Helium, 10 mm, 20.2/30.1°C, machined 304 SS	0.3061	108.48	0.363	0.2838	118.32	0.360
Helium, 10 mm, 20.2/30.1°C, polished 304 SS	0.3056	93.55	0.409	0.2506	122.41	0.387
Argon, 10 mm, 5.2/45.0°C, machined 304 SS	0.1683	20.232	0.875	0.1319	26.266	0.866
Argon, 10 mm, 5.2/45.0°C, polished 304 SS	0.1582	21.95	0.865	0.1175	29.135	0.872
Nitrogen, 5 mm, 15.1/35.1°C, machined 304 SS	0.2152	29.700	0.808	0.1895	34.680	0.795
Nitrogen, 5 mm, 15.1/35.1°C, polished 304 SS	0.2025	32.195	0.800	0.1731	38.571	0.787

5. Conclusions

Heat transfer to surfaces immersed in noncontinuum (transitional or rarefied) gas flow continues to be an active area of research. Gases exhibit noncontinuum effects when the characteristic length scale of the system becomes comparable to the gas mean free path. Thus, these effects become important either when the system length scale becomes small or when the gas pressure becomes low. *A priori* prediction of noncontinuum, gas-phase heat flux requires a detailed description of the gas-surface interaction. Because of the physical complexity of the problem, the most effective approach to providing such descriptions is careful experimental investigations. This LDRD-funded study has provided preliminary experimental data related to the role of surface roughness on thermal accommodation for 304 stainless steel in contact with helium, argon, and nitrogen.

In this study, a previously-developed experimental facility has been used to determine thermal accommodation coefficients from the pressure dependence of heat flux between two parallel plates. Heat flux between the plates is inferred from temperature-drop measurements. The use of high-precision thermistors and the careful control of experimental conditions allow heat-flux measurements to be made with great precision.

Thermal accommodation measurements of argon and nitrogen in contact with standard machined (lathed) or polished 304 stainless steel plates are indistinguishable within experimental uncertainty. Thus, the accommodation coefficient of 304 stainless steel with nitrogen and argon is estimated to be 0.80 ± 0.02 and 0.87 ± 0.02, respectively, independent of the surface roughness within the range likely to be encountered in engineering practice. Measurements of the accommodation of helium showed a slight variation with 304 stainless steel surface roughness: 0.36 ± 0.02 for a standard machine finish and 0.40 ± 0.02 for a polished finish. Planned tests with carbon-nanotube-coated plates will be performed when 304 stainless steel blanks have been successfully coated.

References

Bird, G. A. (1994) *Molecular Gas Dynamics and the Direct Simulation of Gas Flows*, Clarendon Press, Oxford.

Karniadakis, G. E., and Beskok, A. (2002) *Micro Flows: Fundamentals and Simulation,* Springer-Verlag, New York.

Klebanoff, L. E., and Rader, D. J. (2000) "Protection of lithographic components from particle contamination," U.S. Patent #6,153,044, issued November 28.

Liu, C. Y., and Lees, L. (1961) "Kinetic theory description of plane compressible Couette flow," in *Rarefied Gas Dynamics*, L. Talbot, ed., Academic Press, New York, pp. 391-428.

Maxwell, J. C. (1890) *The Scientific Papers of James Clark Maxwell*, Vol. 2, Cambridge University Press, London and New York.

Ohwada, T. (1996) "Heat flow and temperature and density distributions in a rarefied gas between parallel plates with different temperatures," *Physics of Fluids* 8**:** 2153-2160.

Rader, D. J., Dedrick, D. E., Beyer, E. W., Leung, A. H., and Klebanoff, L. E. (2002) "Verification studies of thermophoretic protection for EUV masks," in *Emerging Lithographic Technologies VI,* Roxanne L. Engelstad, ed., *Proceedings of the SPIE* 4688: 182-193.

Rader, D. J., Trott, W. M., Torczynski, J. R., Gallis, M. A., Castañeda, J. N., and Grasser, T. W. (2004) "Microscale Rarefied Gas Dynamics and Surface Interactions for EUVL and MEMS Applications," Sandia National Laboratories report, SAND2004-5329, printed November.

Saxena, S. C., and Joshi, R. K. (1989) *Thermal Accommodation and Adsorption Coefficients of Gases*, Hemisphere Publishing Corporation, New York.

Schaaf, S. A., and Chambre, P. L. (1958) "Flow of rarefied gases," in *Fundamental of Gasdynamics,* Vol. III, H. W. Emmons, ed., Princeton University Press, Princeton, pp. 687-739.

Sherman, F. S. (1963) "A survey of experimental results and methods for the transition regime of rarefied gas dynamics," in *Rarefied Gas Dynamics,* Vol. II, J. A. Lauermann, ed., Academic Press, New York, pp. 228-260.

Springer, G. S. (1971) "Heat transfer in rarefied gases," in *Advances in Heat Transfer,* T. F. Irvine and J. P. Hartnett, eds., Academic Press, New York, pp. 163-218.

Distribution

1	MS 0384	Org. 1500	A. C. Ratzel
1	MS 0825	Org. 1510	W. L. Hermina
1	MS 0834	Org. 1512	J. E. Johannes
1	MS 0834	Org. 1512	C. J. Bourdon
1	MS 0834	Org. 1512	J. N. Castañeda
1	MS 0834	Org. 1512	T. W. Grasser
1	MS 0834	Org. 1512	S. P. Kearney
1	MS 0834	Org. 1512	L. M. Phinney
5	MS 0834	Org. 1512	D. J. Rader
5	MS 0834	Org. 1512	W. M. Trott
1	MS 0826	Org. 1513	S. N. Kempka
3	MS 0826	Org. 1513	M. A. Gallis
1	MS 0826	Org. 1513	E. S. Piekos
3	MS 0826	Org. 1513	J. R. Torczynski
1	MS 0826	Org. 1513	C. C. Wong
1	MS 0834	Org. 1514	J. S. Lash
1	MS 0825	Org. 1515	B. Hassan
1	MS 0836	Org. 1516	E. S. Hertel
1	MS 0836	Org. 1517	R. O. Griffith
1	MS 0836	Org. 1517	R. J. Buss
1	MS 0123	Org. 1011	D. L. Chavez (LDRD Office)
1	MS 9018	Org. 8945-1	Central Technical Files
2	MS 0899	Org. 9616	Technical Library